



Cite This: ACS Cent. Sci. 2019, 5, 1085-1096

http://pubs.acs.org/journal/acsci

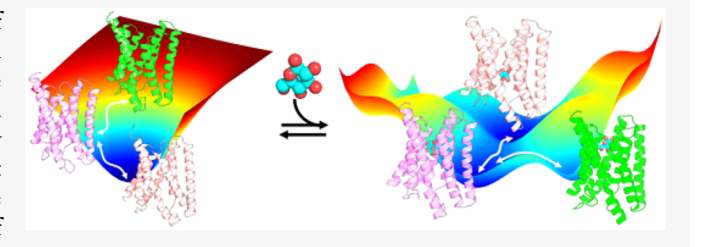
Research Article

Molecular Basis of the Glucose Transport Mechanism in Plants

Balaji Selvam,[†] Ya-Chi Yu,[‡] Li-Qing Chen,[‡] and Diwakar Shukla*,[†],^{‡,§,||,⊥}

Supporting Information

ABSTRACT: The SWEET family belongs to a class of transporters in plants that undergoes large conformational changes to facilitate transport of sugar molecules across the cell membrane (SWEET, Sugars Will Eventually Be Exported Transporter). However, the structures of their functionally relevant conformational states in the transport cycle have not been reported. In this study, we have characterized the conformational dynamics and complete transport cycle of glucose in the OsSWEET2b transporter using extensive



molecular dynamics simulations. Using Markov state models, we estimated the free energy barrier associated with different states as well as for the glucose transport mechanism. SWEETs undergo a structural transition to outward-facing (OF), occluded (OC), and inward-facing (IF) and strongly support an alternate access transport mechanism. The glucose diffuses freely from outside to inside the cell without causing major conformational changes which means that the conformations of glucose unbound and bound snapshots are exactly the same for OF, OC, and IF states. We identified a network of hydrophobic core residues at the center of the transporter that restricts the glucose entry to the cytoplasmic side and acts as an intracellular hydrophobic gate. The mechanistic predictions from molecular dynamics simulations are validated using site-directed mutagenesis experiments. Our simulation also revealed hourglass-like intermediate states making the pore radius narrower at the center. This work provides new fundamental insights into how substrate-transporter interactions actively change the free energy landscape of the transport cycle to facilitate enhanced transport activity.

INTRODUCTION

Sugars are a common source of energy for all living organisms. In plants, sugars are produced through photosynthesis in leaves. The synthesized sugar molecules are transported to different tissues and organelles through a class of specialized cellular uptake transporters called SWEETs (Sugars Will Eventually Be Exported Transporters). SWEETs are a family of transporters that have been recently identified in plants and mediate various physiological functions including plant growth, nectar production, and seed and pollen development.^{2,3} SWEETs transport diverse substrates including glucose and sucrose which is involved in long-distance sugar transport through a phloem loading mechanism from the source (leaves) to sink (fruits, roots) tissue. 4-6 Thus, engineering SWEETs to increase the sugar loading in phloem could enhance the crop yield. SWEETs are also involved in many developmental processes. Therefore, it is important to understand their functional role and transport mechanism to meet current challenges in agricultural productivity.

SWEETs consist of seven transmembrane (TM) helices arranged into a pair of triple helix bundles (THBs) connected by an inversion linker, namely, TM4. These transporters share close structural homology with the bacterial sugar transporters SemiSWEETs, 8-10 the smallest transporter protein. 11 Evolutionary sequence analysis reveals that SWEETs and Semi-SWEETs belong to the PQ-loop family of transporters characterized by a conserved Pro-Gln motif in TM1. 12 Crystal structures of SemiSWEETs in different conformational states [i.e., inward-open (IF),10,13 occluded (OC),9 and outward-open (OF)^{10,13} state] have provided the opportunity to understand the functional mechanisms of these proteins in atomistic detail. The distinct conformations of SemiSWEETs highlight that its transport mechanism is based on the principle of alternate access. 14 However, the crystal structure of the SWEET family transporter, OsSWEET2b, has been obtained in the IF state, 15 which is the first structure of a sugar

Received: March 12, 2019 Published: May 29, 2019



Department of Chemical and Biomolecular Engineering, University of Illinois at Urbana-Champaign, Urbana, Illinois 61801, United States

[‡]Department of Plant Biology, University of Illinois at Urbana-Champaign, Urbana, Illinois 61801, United States

[§]Center for Biophysics and Quantitative Biology, University of Illinois at Urbana-Champaign, Urbana, Illinois 61801, United States $^{\parallel}$ NIH Center for Macromolecular Modeling and Bioinformatics, University of Illinois at Urbana-Champaign, Urbana, Illinois 61801, United States

[⊥]Beckman Institute for Advanced Science and Technology, University of Illinois at Urbana-Champaign, Urbana, Illinois 61801, United States

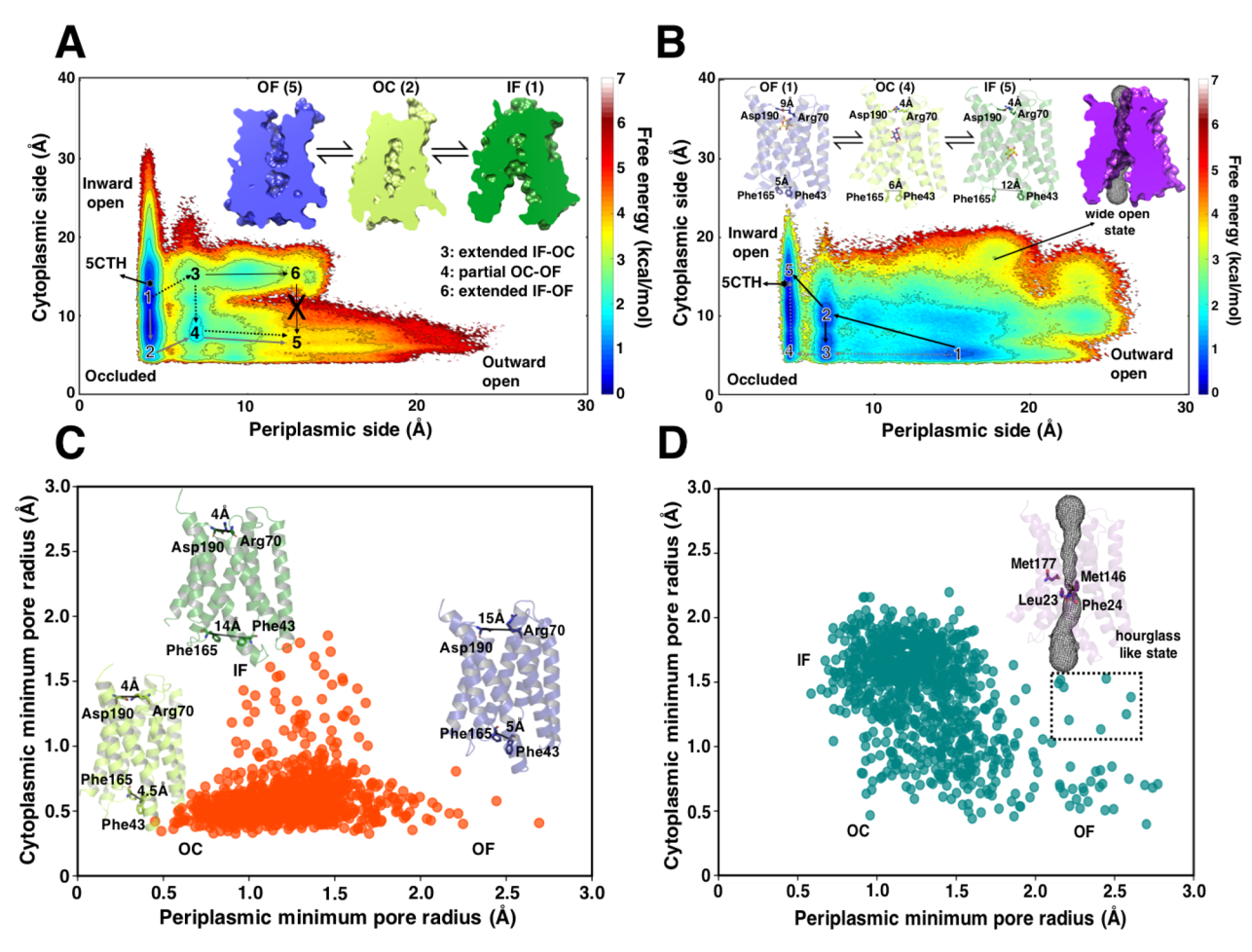


Figure 1. Conformational free energy landscape of OsSWEET2b. The free energy landscape plot for OsSWEET2b (A) without and (B) with glucose. The pore channel gating residues opening and closure at the periplasmic and cytoplasmic side are obtained by measuring the distances between the residue atoms Asp190 (CG)–Arg70 (CZ) and Phe165 ($C\alpha$)–Phe43 ($C\alpha$). The crystal structure (PDB ID: 5CTH) is shown as a black star. The glucose induced conformational changes in OsSWEET2b are shown in part B. The changes in pore radius and glucose translocation at different conformational states are depicted in parts A and B. The average pore channel radius for all states is shown for glucose unbound and bound simulations in parts C and D. (D) The hourglass-like intermediate state shows that the pores are open at both ends and constricted at the middle of the transporter.

transporter in plants. In the available crystal structure of OsSWEET2b, the binding site is occupied by polyethylene glycol (PEG). 15 The chemical group oxyethylene mimics the sugar (hydroxyl moiety), and the bound pose of PEG is stabilized by weak van der Waals interaction. It is likely that the oxyethylene moiety mimics the glucose in the binding site. 10,15 However, a single crystal structure cannot provide an understanding of the intermediate metastable states and the transport cycle of SWEETs. Furthermore, it remains unclear how SWEETs or any other plant sugar transporters recognize, bind, and translocate glucose in plants. More recently, the crystal structure of AtSWEET13 was also obtained in the IF state bound to a 2'-deoxycytidine 5'-monophosphate in the central binding site.¹⁶ Both OsSWEET2b and AtSWEET13 share a similar structural topology. To characterize the complete transport cycle, the structural knowledge of intermediate states such as OC and OF states is essential to elucidate the molecular mechanism of membrane transporters.

A recent molecular simulation study of LbSemiSWEET proposed a "free-ride" mechanism of glucose transport, where the term "free-ride" was used to imply that glucose diffuses freely from the extracellular to intracellular side without inducing major conformational changes in the transporter.¹³

From a structural viewpoint, there are no major helical shifts while glucose is being transported. It is not clear if a similar mechanism applies to the SWEET transporters as well. In this study, we used computational approaches to not only test the applicability of the "free-ride" mechanism to the structures of the intermediate conformational states (OC and OF) of the SWEETs but also provide an atomistic description of the glucose binding mechanism and the gating residues responsible for locking the transporter in specific conformations. We used the glucose unbound OsSWEET2b monomer in the IF state as a starting structure and performed extensive molecular dynamics (MD) simulations to capture the molecule-level details of transitions among conformational states. Using Markov state models (MSMs), we cluster the simulation data into kinetically relevant states and estimated the free energy barrier to the conformationally distinct state and also characterized the complete glucose transport cycle. The critical residues that participate in transport identified using simulations are validated using site-directed mutagenesis experiments. Mutations in AtSWEET1 designed on the basis of the mechanistic insights from simulations abolish (Asn50) or exhibit dramatic effects (Tyr44, Glu80, Cys172, and Tyr189) on glucose transport. From MD simulations of

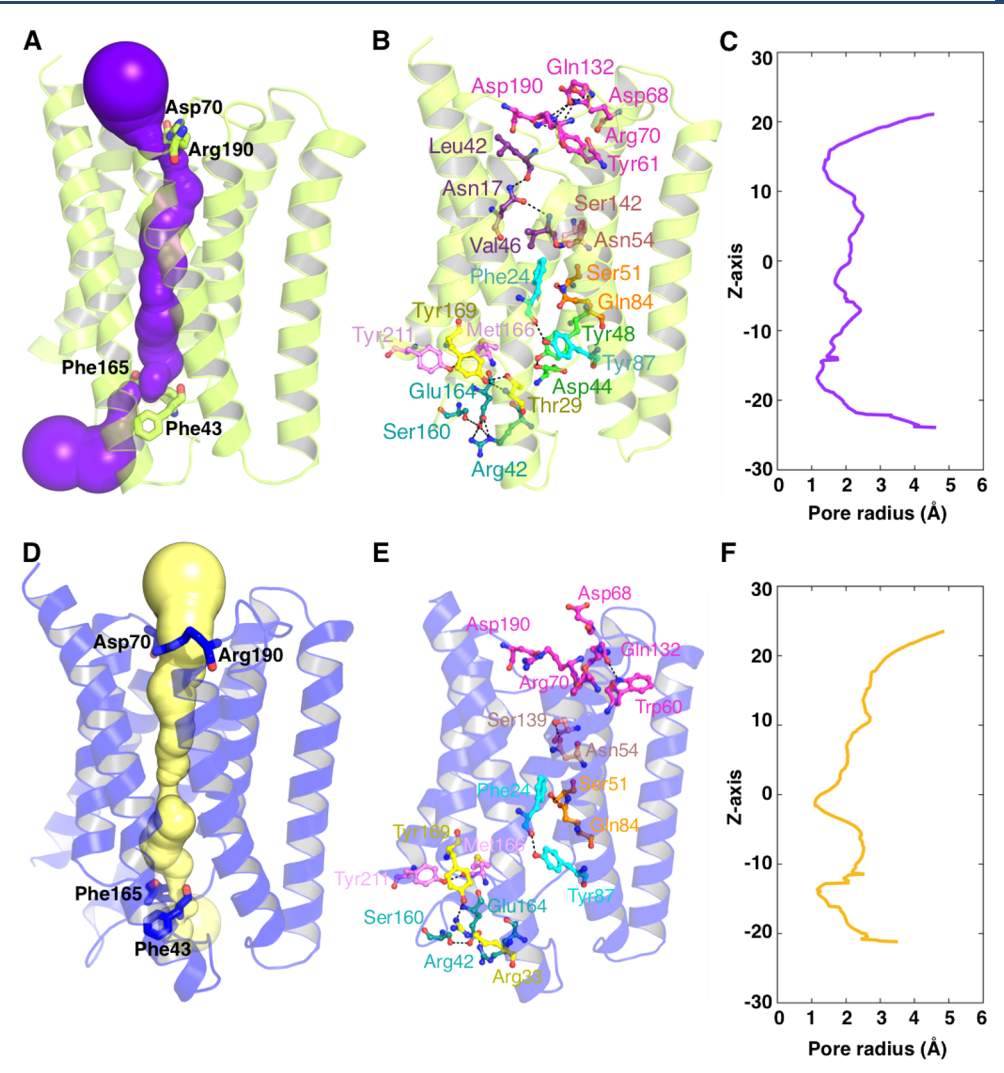


Figure 2. Structural characteristics of the predicted (A–C) OC and (D–F) OF state. The pore channel passing through the predicted OC and OF state is shown in (A) purple and (D) yellow. The interhelical interaction that stabilizes OC and OF states is depicted in parts B and E. Two-dimensional plot of the pore channel radius along the Z-axis obtained for the (C) OC and (F) OF state using the HOLE program. The snapshots corresponding to OC and OF microstates are extracted from the simulation data, and the average pores channel radius is shown for both states, respectively (see the Methods and Materials section for details).

glucose bound OsSWEET2b, we show that glucose diffuses freely from the periplasmic to cytoplasmic side in SWEETs without inducing major conformational changes, but glucose molecules actively remodel the free energy landscape by lowering the energy barrier between the intermediate states to enhance the transport. Our results raise interesting questions about the structural and functional design of SWEET transporters that enable this mechanistic difference from its structural and functional homologue in bacteria, SemiSWEETs.

RESULTS

Glucose Reduces the Free Energy Barrier Associated with the Transport Process in OsSWEET2b to Enhance its Transport Rate. The OsSWEET2b crystal structure (PDB ID: 5CTH), ¹⁵ obtained in the IF state, was used as the starting structure for MD simulations. Simulations were performed over a duration of ~213 μ s to explore the conformational landscape of glucose unbound ($apo \sim 145 \mu$ s) and bound ($holo \sim 68 \mu$ s) transporter. The glucose unbound data set was used to build an MSM (see the Methods and Materials section for details), and the MSM equilibrium probability weighted

free energy landscape plot reveals the key transition among states (Figure 1A). The ionic interaction between Asp190 (CG)-Arg70 (CZ) at the periplasmic side acts as a lid and closes the pore tunnel. At the cytoplasmic side, a residue on the loop that joins TM1-TM2 (Phe43 (C α)) and another residue on the loop that joins TM5-TM6 (Phe165 (C α)) act as an intracellular gate (Figure S1). We projected the simulation data on these two metrics to explore the conformational dynamics of the transporter as the opening and closure of pore channels strictly determine the specific state such as OF, OC, and IF. The states 1-6 in Figure 1A represent the inward-open (IF), occluded (OC), extended IF-OC, partial OC-OF, outward open (OF), and extended IF-OF states. The dominant pathways of conformational transition between the intermediate states were identified using transition path theory (TPT). The gray solid line in the plot shows the lowest free energy pathway between the IF and OF states, while an alternate, higher-free-energy pathway is shown with black dotted arrows. The thin solid black lines show the extended wide open IF-OF state, and transition through this pathway is not possible because of the high energy

barrier. The free energy barrier for one complete cycle of glucose unbound OsSWEET2b from the IF to OF state was found to be ~4 kcal/mol.

In glucose unbound simulations, the distances between the loops at the cytoplasmic side increase up to \sim 30 Å leading to a high-energy unstable state (~5 kcal/mol) (Figure 1A). The loops come close to each other as TM2 and TM6 become straight, thus leading to the formation of the OC state. The cytoplasmic distance reduces to ~4-5 Å, and the free energy plot shows that $\sim 0.5-1$ kcal/mol is required to switch from the IF to the OC state. The partial OC-OF state is obtained as Arg70 loses interaction with Asp190 and the distance between the residues increases to $\sim 7-9$ Å. A free energy of $\sim 3-3.5$ kcal/mol is required for the transition from the OC to the partial OC-OF state. A further increase in the same distance to \sim 15-20 Å results in the OF state. The transporter also adopts an extended IF-OC conformational state, where the intracellular distances are equivalent to the crystal structure; the extracellular distances increased to ~7-9 Å, and the OF state is finally reached via the partial OC-OF state. The free energy barrier for the transition from the IF to the extended IF-OC was found to be ~3-3.5 kcal/mol which is higher compared to Path-1A. The conformations like extended IF-OF are also obtained, and it is evident from the conformational landscape plot that the transitions through this state are restricted due to the high energy barrier. The measurement of minimum pore radius of different states reveals that SWEETs follow the canonical alternate access mechanism (Figure 1C).

The simulations were further extended from the OF state to investigate the glucose binding and transport mechanism (Figure 1B), and a similar MSM analysis was performed on the collected MD data (see the Methods and Materials section for details). TPT identified two dominant paths, and the path indicated by the gray dotted line shows the glucose transported from the OF to IF state via the partial OC-OF and OC state. The path indicated with the black line shows glucose transport via extended IF-OC state. In the presence of glucose, the landscape becomes flat with a highest barrier of ~3 kcal/mol, and intermediate states are easily accessible compared to those in glucose unbound simulations. The free energy plot shows that the glucose bound simulations stabilize the OF state with an energy difference of ~2 kcal/mol as compared to the unbound OF state. For glucose bound OsSWEET2b, the free energy barrier for transition both from the partial OC-OF to the OC state and from the extended IF-OC to the IF state was $\sim 2-3$ kcal/mol. The comparisons of mean pore radius and structures of IF, OC, and OF states of bound simulations are similar to unbound simulations (Figure 1D and Figures S13). The presence of glucose also results in the sampling of hourglass-like intermediate states where the transporter is open at both ends and narrower at the center. The adaptation of intermediate hourglass-shaped cavities is one of the common structural topologies in membrane transporter biology to transport substrate molecules. 20,21 However, the average pore radius for hourglass-like states shows that the pores are constricted at the center of the transporter, thereby maintaining the alternate access mechanism instead of showing channel-like behavior (Figure 1D).

Rearrangement of the Hydrogen Bond Network Enables the Transition between Conformational States of the SWEET transporter. The predicted OC state exhibits large structural changes in the cytoplasmic side compared to the periplasmic side. Figure 2A shows that the pore channel is

closed at both ends of the transporter. The polar and the ionic residues (Asp190, Arg70, Tyr61, Gln132) form a network of strong interaction at the periplasmic side to close the pore channel. The guanidinium group of Arg70 interacts with the carboxylate group of Asp190, acting as an extracellular gate (Figure 2B). This salt bridge interaction is conserved in LbSemiSWEET (Figure S7A-C) . Arg55-Asp57 in LbSemi-SWEET⁹ (Figure S7C) acts as gating residues which lock the transporter at the periplasmic side. The disruption of this ionic interaction leads to the OF conformation. 13 Tyr61 of TM2 makes an additional hydrogen bond interaction with Asp190, and the conformation of Tyr61 is further stabilized by Gln132 of TM5. These amide and hydroxyl interactions close the extracellular opening and further stabilize the conformation. Tyr51 (Tyr61)-Asp57 (Asp190) residue interactions are also conserved in LbSemiSWEET, and this additional polar interaction locks the helices in a closed conformation. ⁹ The interhelical polar interactions between the residues Asn17-Leu72 (CO), Asn17-Val76 (NH), and Asn54-Ser142 (OH) at the extracellular side are very similar to those in the crystal structure (IF). 15 TM2 becomes straight and establishes a new hydrogen bond interaction between Gln84 and Ser51 (OH), thus stabilizing the helix conformation. The distance between Pro47 (C α)-Ser171 (C α) and Tyr48 (C α)-Leu170 (C α) at TM2 and TM6 reduces to \sim 12–13 Å compared to \sim 17 Å in the IF state (Figure S7H). The corresponding residues [Tyr38] (protomer A)-Met37 (protomer B) and Met37 (protomer A)-Tyr38 (protomer B)] on TM2 (A)-TM2 (B) in the LbSemiSWEET (OC) crystal structure are 13.7 Å away from each other (Figure S7G). This helical movement partially closes the intracellular side of the transporter. The intracellular loops come close to $\sim 4-5$ Å as the transporter approached the final OC state. The loops were further held tight by formation of ionic/polar contacts between Glu164-Arg42-Ser160 which stabilize the loop conformation that locks in the OC state. The distance between the loop joining residues [Asp32(C α -A)-Asp $32(C\alpha$ -B) and Phe $43(C\alpha)$ -Phe165(C)] in LbSemi-SWEET and predicted SWEET (OC) are $\sim 4-5$ Å, respectively (Figure S7D). The predicted OC state aligns well with LbSemiSWEET (OC) (Figure S7B,F), which is demonstrated by similar pore radius profiles (Figure S7E). The interhelical hydrogen bond interactions Gln84-Ser51 (TM3-TM2), Tyr48-Asp44 (TM1-loop), Tyr87-Phe24 (TM3-TM1), Tyr169-Thr29 (TM6-TM1), and Tyr211-Met166 (TM7-TM6) provide additional stability to the OC state.

Large helical rearrangements at the extracellular side of the transporter were identified in the predicted OF state as compared to the crystal structure, and few changes were noticed at the intracellular side (Figure 2D). The pore channel radius of the predicted OF state and the EcSemiSWEET crystal structure 10 (OF) shows that the periplasmic cavities are wide open while the intracellular parts are closed (Figure S8A). Breakage of ionic and polar interactions between Arg70-Asp190, Asp190-Tyr61, and Tyr61-Gln132 results in extensive movement of TM2, TM3, TM6, and TM7. The helices TM2 and TM6 move ~15-20 Å from each other and open the pore channel (Figure 2E and Figure S8B). The OF states are less stable as the free energy of this state ($\sim 3-4$ kcal/mol) is higher than those of the other intermediate states (Figure 1A). The interaction Gln132-Trp60 stabilizes TM2 in the OF state. TM2 rotates ~5 Å, and thus, Asn54 loses interaction with Ser142 establishing a new contact with Ser139, thereby providing additional support for opening of

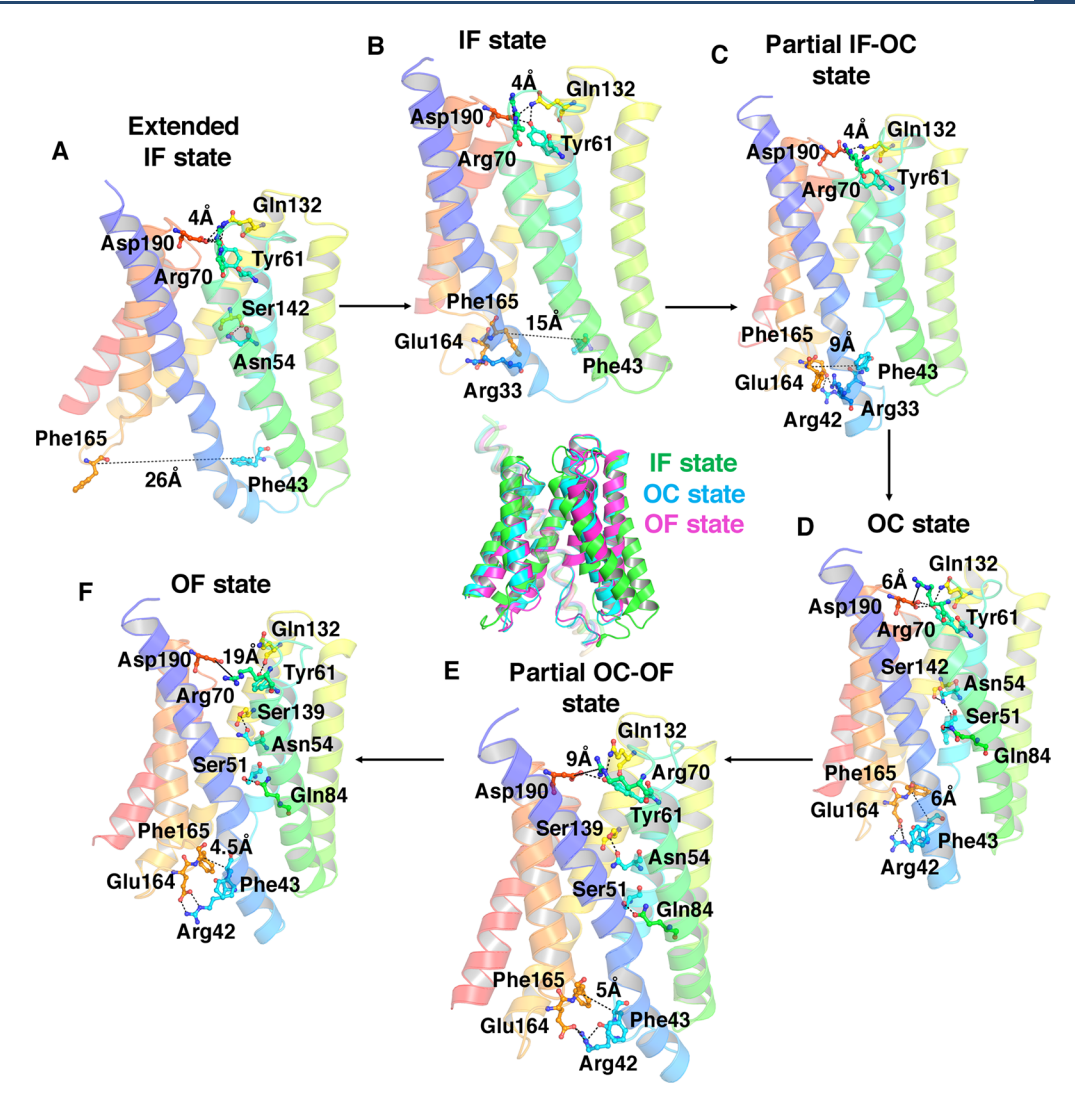


Figure 3. Conformational switches characterized using TPT for glucose unbound simulations. The structural transitions from IF to OF via intermediate states are shown in parts A–F. (A) Extended IF. (B) IF. (C) Partial IF–OC. (D) OC. (E) Partial OC–OF. (F) OF. The distance between the gating residues and key polar interaction between the crucial residues that drives the structural changes are shown in black dashed lines.

the pore channel at the periplasmic side. The interactions at the intracellular part of the receptor are retained as observed in the predicted OC state. The hydrogen bond contacts between the residues Gln84-Ser51 (TM3-TM2), Tyr87-Phe24 (TM3-TM1), Tyr169-Arg33 (TM6-TM1), and Tyr211-Met166 (TM7-TM6) keep the helices close to each other and partially close the bottom part of the transporter. Additionally, the loop residues Glu164-Arg42-Ser160 form a polar interaction and close the transporter at the cytoplasmic side in the OF state. The EcSemiSWEET (OF) crystal structure and the predicted OF state are in good agreement in terms of localization of helices (Figure S8B-D,F). The OF state pore radius plot shows a good match with EcSemiSWEET (Figure 2F and Figure S8E). The comparison of intracellular distance between the helices TM2 (protomer A)-TM2 (protomer B) of the EcSemiSWEET (OF state) crystal structure is in good agreement with the predicted OF state (Figure S8G,H).

Conformational Transition in the Glucose Unbound Simulation. Using transition path theory (TPT), we determined the conformational transitions between intermediate states that dominate in the transport cycle of OsSWEET2b

(Figure 3). TPT identifies the top flux pathways from the IF (source) to OF (sink) state through intermediate states in the MSM (Figure S9A,B). In MD simulations, we observed the extended IF state, where the cytosolic loops at the intracellular part increase up to ~25-30 Å and result in an energetically unstable state (Figures 3A and 1A). The network of polar hydrogen bond interactions closes the pore channel at the periplasmic side. In the IF state, TM1 is kinked at Pro27 and results in a bendlike helix conformation. The proline residue is conserved in SemiSWEET and SWEET, and mutation to alanine in EcSemiSWEET decreases substrate transport. 10,15 The distance between the cytoplasmic loops decreases to 9 Å and forms the salt bridge interaction of Glu164-Arg33, thereby initiating the conformational transition from IF to partial IF-OC (Figure 3B,C). The network of polar hydrogen bond interactions closes the pore channel at the periplasmic side. In the IF state, TM1 is kinked at Pro27 and results in a bendlike helix conformation. The proline residue is conserved in SemiSWEET and SWEET, and mutation to alanine in EcSemiSWEET decreases substrate transport. 10,15 The distance between the cytoplasmic loops decreases to ~9 Å and

forms the salt bridge interaction of Glu164-Arg33, thereby initiating the conformational transition from IF to partial IF-OC (Figure 3B,C). The shift in the salt bridge interaction between Arg33-Glu164 to Arg42-Glu164 further decreases the loop distance to \sim 4–6 Å resulting in the OC state (Figure 3D). In the OC state, the polar interactions at the periplasmic side are analogous to the IF state, and TM1 becomes more straight compared to the kinked helix in the IF state. The additional helical contact between Gln84-Ser51 on TM2-TM3 adds more stability to the helices to adopt the OC state. The formation of stronger interactions at the cytosolic surface results in weakening of the interaction at the periplasmic surface. The breakage of the Arg70-Asp109 ionic interaction results in the partial OC-OF state (Figure 3E). In the partial OC-OF state, the distance between the Arg70-Asp190 increases to ~7-9 Å and partially opens the extracellular cavity. At this juncture, Tyr61 still holds the interaction with Asp190, stabilized by the interaction between Tyr61-Gln132. The distance between Arg70-Asp190 further increases up to ~19 Å to obtain a final OF state (Figure 3F). Tyr61 loses its interaction with Asp190 and Gln132 to obtain the final OF state. The phenol ring of Tyr61 shifts down and interacts with Gln132 (CO) stabilizing the conformation of TM2. The sliced surface representation of intermediate states shows the change in pore channel radius during the conformational transition from one state to the other (Figure S10A-F).

Structural Dynamics of apo and holo OsSWEET2b. The simulation provides the global structural flexibility of the individual amino acids. The root mean-squared fluctuation (RMSF) calculation of apo and holo OsSWEET2b simulations enables us to determine the segments of the transporter that are crucial for conformational dynamics and substrate transport. The intra- and extracellular loops are highly flexible in both apo and holo simulations (Figure 4A,B). The helices 3, 4, 5, and 6 are very dynamic in holo in contrast to apo revealing

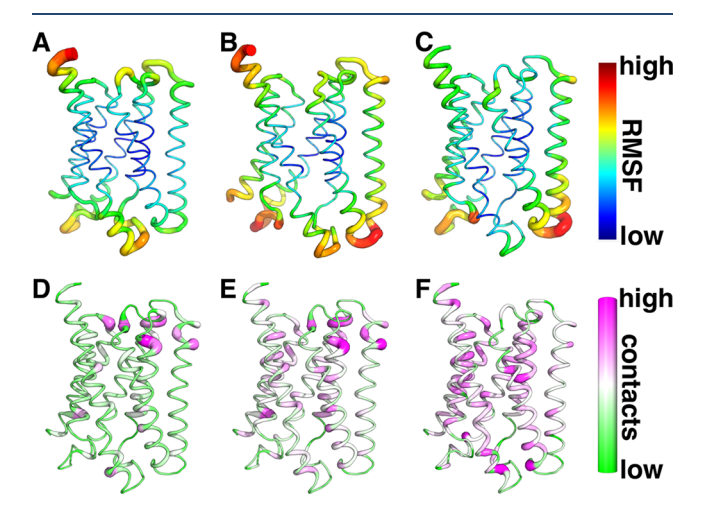


Figure 4. Molecular dynamics analysis of global fluctuations of *apo* and *holo* OsSWEET2b. Root mean-squared fluctuations (RMSFs) of the (A) *apo* and (B) *holo* transporter from the crystal structure. (C) Difference between the RMSF of the *apo* and *holo* transporter from the crystal structure. Tube thicknesses correspond to the RMSF values for each residue. The residue—residue contacts for each residue in the (D) *apo* and (E) *holo* transporter. (F) Difference between the residue—residue contacts for the *apo* and *holo* transporter. The tube thickness shows the frequency of the contacts for a particular residue in the transporter.

that the presence of glucose increases the flexibility of the transporter (Figure 4C, Figure S11A,B). The helix 2 was relatively stable in both simulations as compared to other helices (Figure S11A,B). To identify the crucial residues that drive the conformational transition, we calculated all possible residue-residue contacts for both apo and holo, shown as a Debye-Waller factor (Figure 4D-F). The high residual contacts are noticed at the extracellular region in both apo and holo (Figure 4D-E) which shows that key ionic and polar interactions stabilize OC and IF states. The residues in the transmembrane domain 2 and 6 and the intracellular loops IL1/IL3 form key hydrogen bond contacts and are involved in a structural transition to different conformational states. However, the high residue-residue interactions are noticed for holo in these regions compared to apo. One possible reason could be that in apo simulation the residues freely access the void space inside the channel pore while, in the glucose bound (holo) system, the residue and substrate are strongly coupled to form a favorable interaction that leads to structural changes and a transport mechanism. To determine the substrate (glucose) induced conformational transition and transport, we studied the complete glucose transport mechanism in OsSWEET2b.

Intracellular Hydrophobic Gating Residues Act as a Conformational Barrier to Glucose Translocation. We characterized the glucose transport mechanism in OsS-WEET2b by initializing the simulation from the OF state over a period of \sim 68 μ s. We determined the conformational driven glucose translocation and the transport cycle of OsSWEET2b (Figure 5). TPT identifies the top flux pathways from the IF (source) to OF (sink) state through intermediate states in the MSM using TPT. The kinetics plot shows that the time required for one complete glucose transport cycle is estimated as \sim 6 μ s (Figure 5 and Figure S12). The average mean first passage time (MFPT) for the glucose translocation was determined as \sim 6.4 \pm 0.3 μ s by TPT. The guanidinium group of Arg189 recognizes the glucose molecule and initiates substrate transport (Figure 5A). The gating residues are \sim 15 Å apart and favor glucose binding at the periplasmic side. Asp190 coordinates with glucose, thereby facilitating transport to the extracellular surface, and forms stable contacts with Arg70 and Asp68. The distance between gating residues decreases to 10 Å as the polar interaction tightens the extracellular cavity (Figure 5B). The glucose diffuses to the pore channel through Tyr184, Asn197, Tyr61, and Arg70 (Figure 5C), and this results in the closure of the transport channel at the extracellular part of the transporter. The glucose is stabilized by Asn197 and Asn77 in the binding site, and mutation of these residues to alanine reduces the glucose uptake in SWEETs and Semi-SWEET. 8-10,13,15 At this juncture, the transporter is closed at both ends to obtain the OC state (Figure 5D). The intracellular hydrophobic gating residues Phe24 (TM1)-Met146 (TM5)-Met177 (TM7) act as a barrier for the glucose and restrict further movement. The formation of a strong electrostatic interaction (Asp190-Arg70-Tyr61-Gln132) at the extracellular part of the transporter (Figures 5D and 3B) weakens the hydrophobic gate; as a result, the intracellular gating residues start moving away from each other.

The displacement of the intracellular gating residues (Phe165–Phe43) to 9 Å from each other increases the distance between the hydrophobic gating residues allowing glucose to enter the intracellular part of the transporter (Figure 5E). Ser51, Asn54, and Asn77 coordinate with glucose to

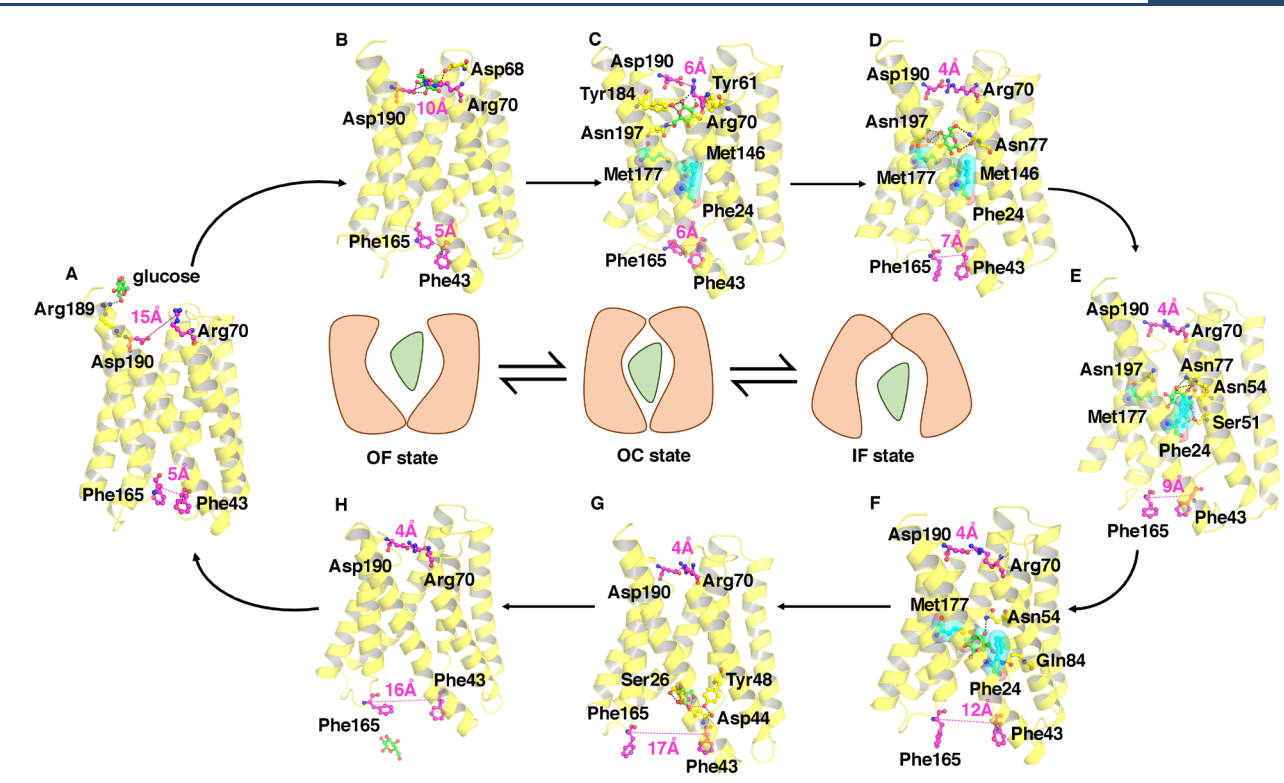


Figure 5. Simulation of the binding of the glucose molecule to OsSWEET2b. The glucose binding mechanism and the glucose driven conformational changes are shown in parts A–H. (A–C) In the OF state, glucose binds to OsSWEET2b. (D) Structural transition to OC and glucose stabilized at the binding site. (E–F) The opening of the intracellular gate and glucose slides down to cytosolic loops. The distance between gating residues [Arg70 (CZ)–Asp190 (CG) and Phe165 ($C\alpha$)–Phe43 ($C\alpha$)] are shown in magenta. The intracellular hydrophobic gates Phe24–Met146–Met177 are shown in cyan. The glucose molecule is shown in green.

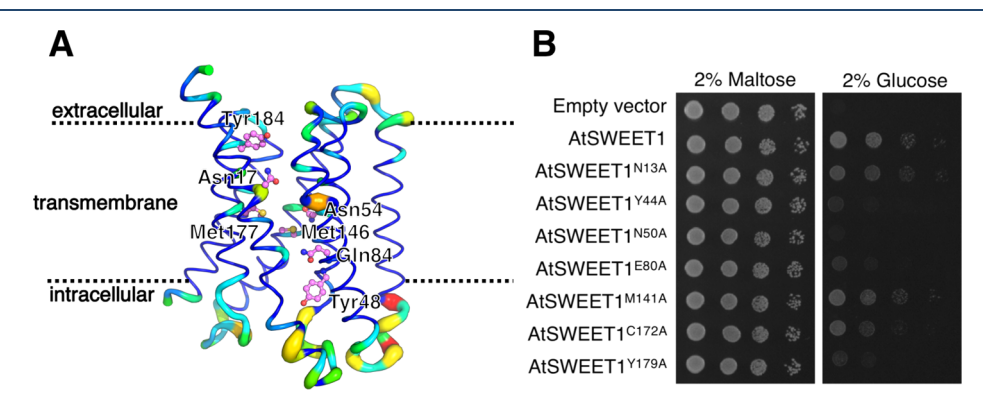


Figure 6. Prediction and validation of crucial residues along the transport pathway. (A) Computation predictions of crucial residues in the glucose transport pathway. The tube thickness shows the frequency of the contacts. (B) Functional analysis of mutant AtSWEET1 by complementation of the yeast growth assay. N13A and M141A have little effect on transporter activity. C172A, Y44A, E80A, and Y179A have dramatic effects on the activity and significantly reduce yeast growth. N50A abolishes activity completely.

overcome the hydrophobic barrier (Phe24–Met146–Met177). Ser51 is replaced by Thr47 in AtSWEET1 and plays a crucial role in sugar transport. Glucose slides down and forms a hydrogen bond interaction with Gln84, which further opens the intracellular gates of the transporter to \sim 12 Å (Figure 5F and Figure S12). Finally, the transporter reaches the IF state as the distance between the gating residues increases to \sim 17 Å, and glucose interacts with Ser26, Asp44, and Tyr48 and leaves the transporter (Figure 5G,H). The comparison of IF, OC, and OF states of glucose unbound and bound simulations reveals that SWEETs translocate glucose freely as SemiSWEETs¹³ (Figures S13 and S14). Although, in glucose bound simulations, we obtained hourglass-like

intermediate states, the measurement of the mean pore radius shows that the pore is constricted at the intracellular hydrophobic gate which restricts the channel-like leaks thereby maintaining the alternate access transport mechanism. We also compared the $C\alpha$ distance between the hydrophobic gating residues in IF, OC, and OF states of SWEETs, in good agreement with the IF, OC, and OF SemiSWEET structures (Figure S15).

Simulation Identifies Key Sensitive Residues and Predicts Deleterious Mutation. To determine the role of crucial residues in the glucose binding and transport, we computed noncovalent interactions such as H-bonds and aromatic and weak hydrophobic interactions using GetCon-

tacts software.²³ We identified the critical residues in the extracellular (Tyr184), transmembrane domain (Asn17, Asn54, Gln84, Met146, and Met177), and intracellular (Tyr48) region that drives the glucose uptake and transport mechanism. We validated our computational predictions using site-directed mutagenesis experiments. Our MD analyses show that Tyr184 is involved in the extensive polar and hydrophobic interaction with glucose and accelerates movement to the center of the transporter. Our experimental findings show that the mutation of Tyr179 to alanine in AtSWEET1 had a dramatic effect on transport activity (Figure 6B). The earlier studies indicated that the mutation of Tyr179A in AtSWEET1 has little effect on the transport activity; 24,25 however, we have shown that Tyr184 is one of the crucial residues involved in the transport process (Figure 5C). Asn17 to alanine has no significant effect on glucose transport. We predicted that Asn54 points toward the transport channel during the conformational driven glucose transition and forms a crucial hydrogen bond contact with glucose. Our experiments show that the substitution of Asn50 to alanine abolishes the transport activity in AtSWEET1 (Figure 6B). The evolutionary sequence analysis performed using ConSurf²⁶ reveals that Tyr179 and Asn50 are conserved across the SWEET family (Figure S16). We also mutated the key hydrophobic gating residues that form a weak van der Waals interaction with glucose during the transport cycle. The mutation of Met141 with alanine has little effect while Cys172 to alanine has a significant effect on the glucose transport activity (Figure 6B). Gln84 is replaced by Glu80 in AtSWEET1 and other AtSWEET subtypes except AtSWEET2 and AtSWEET10, and the mutation of Glu80 to alanine leads to a complete loss in the transport activity (Figure 6B and Figure S16). Tyr48 at the intracellular region is conserved across the SWEET family and forms a van der Waals interaction as well as a polar interaction with glucose during the exit pathway. The mutation of Tyr44 in AtSWEET1 disrupts the transport activity as is consistent with our simulation predictions. The residues reported in our study are unique, play a major role in the glucose transition, and were not known earlier, and it is not possible to obtain these data without simulating the complete glucose transport pathway. The sliced surface representation shows that the center hydrophobic region is conserved in the SWEET family compared to the extracellular and intracellular region (Figure S17).

CONCLUSION

Our study reveals in atomistic-level detail the conformational transitions constituting the OsSWEET2b transport cycle as well as the free energy landscape associated with the entire process. We also characterized the complete glucose transport mechanism from the extracellular to the intracellular side of the plasma membrane for the first time for any plant transporter using extensive unbiased simulation. MSM weighted conformational plots of the glucose unbound simulation show that a free energy barrier of ~4 kcal/mol is required for one complete cycle from the IF to OF state. The conformational switch from IF to OC requires less free energy, and the transition from OC to OF via the partial OC-OF state has a higher free energy

The free energy barrier between various states for glucose bound simulations is less compared to that for unbound simulations, and our MD study shows that the glucose molecule changes the conformational landscape of the

transporter. Glucose transport pathways show a barrier of ~3 kcal/mol to switch from the intermediate to the IF state. The presence of glucose reduces the free energy barrier of the transporter to $\sim 1-2$ kcal/mol. The crystal structure of OsSWEET2b was determined in the IF state, and our MD study agrees with structural studies showing that IF is one of the most stable states of the transporter. The predicted OC state is also relatively stable in both simulations. In the holo simulation, we observed greater stability of the OF state which is in contrast to the lesser stability in the apo simulation. The glucose molecule forms an energetically favorable interaction and diffuses to the cytoplasmic half. The exchange of the hydrogen bond interaction network between glucose and polar residues around the pore channel drives the conformational change and the transport process. In the absence of substrate, the water molecules coordinated with residues and favor structural rearrangements which may be a relatively slower process compared to the substrate bound instance. Hence, the combined glucose-water effect shifts the conformational equilibrium of intermediate states to enhance the transport. The lowering of the activation energy in the presence of ADP/ ATP was shown in ADP/ATP carrier proteins using welltempered metadynamics.²⁷ The simulation of LeuT in the presence of leucine with the sodium ion also shows that the substrate bound simulation samples more wide conformations compared to *apo* simulations.²⁸ We captured the complete cycle of glucose translocation in OsSWEET2b and predicted the key residues that play a significant role in the transport mechanism. We also validated our predictions using mutagenesis experiments, and the results show that our predictions play a significant role in the transport mechanism.

SWEETs are passive transporters that transport substrate molecules through facilitated diffusion. During photosynthesis, the main product is glucose, and it is rapidly accumulated in the leaves; it needs to be efficiently transported to different tissues. SWEETs facilitate the transport of sugar molecules from leaves to phloem. Our study shows that the binding of glucose flattens the free energy conformational landscape of the SWEET transporter. In other words, the transport process becomes more energetically favorable in the presence of glucose. The improved efficiency of glucose bound transporters would facilitate the efficient distribution of sugar molecules to various tissues with limited energetic cost. The lowering of the free energy barrier only in the presence of the substrate would also hinder the transport of other molecules thereby enhancing the selectivity of the transporter.

The comparison of the glucose transport mechanism in SWEET and SemiSWEET shows a similar pattern of substrate translocation. Although few MD studies on SemiSWEETs are reported in the literature, the complete substrate transport mechanism was not fully characterized. 13,29 The extracellular residues in SWEET and SemiSWEET play a crucial role in glucose recognition and the transport mechanism. The conserved Tyr61 (TM2) and Tyr184 (TM7) form key contacts at the periplasmic side, and mutation to alanine leads to the loss of function in both SWEET and Semi-SWEET^{13,15} (Figure S15). The glucose molecule is stabilized in the binding site by Asn77 and Asn197, and these residues are fully conserved across the SWEET and SemiSWEET family of transporters 13,15,29 (Figure S16). Multiple studies show that mutation of these residues abolishes the glucose uptake (Table S4).^{8–11,15} The glucose bound MD snapshot of SWEET shows good agreement with the substrate bound SemiSWEET

(Figure S18). The evolutionary sequence alignment of SWEETs shows that these residues are conserved across the family (Figure S16). Bera et al. show that Thr15 at the binding site provides additional stability to the glucose whereas the equivalent residue in SWEET is hydrophobic; however, the Asn54 in TM2 forms a favorable contact to stabilize the glucose molecule adjacent to the binding site. The sequence analysis of SWEET also reveals that the conserved hydrophobic intracellular gate acts as a barrier for the glucose to enter the cytoplasmic side (Figure S17). The bulky aromatic Phe17 (TM1) and Phe41 (TM3) act as a barrier for glucose entry in LbSemiSWEET; 13 however, the mutation of equivalent residues in SWEETs leads to a dramatic effect (Figure 6B). In SWEET, we identified that Gln84 (TM3) forms a key polar contact at the transient state before the glucose slides down to the loop region; in contrast, the equivalent residue in SemiSWEET is hydrophobic. Upon opening of the cytoplasmic half, the glucose diffuses to the intracellular side by forming polar contacts with TM1 residues in both SWEET and SemiSWEET.²⁹ The passive glucose transporter was also reported in humans which plays a crucial role in pathophysiological functions; however, the previous studies used a nonequilibrium approach to understand the substrate translocation from the binding site, as obtaining an unbiased landscape for the complete transport cycle is computationally expensive. 30,31

To our knowledge, this is the first unbiased computational study that captured the conformational dynamics and the intermediate states of SWEETs. We also explored the glucose transport mechanism by initializing the simulation from the OF state. We found that the large cytoplasmic opening of the intracellular gates is not required for the glucose, as the molecule is small enough to escape when the pore is partially open. However, it may not be true for larger substrates such as sucrose or fructose. SWEETs form functional oligomers and transport substrate molecules. We have investigated that the monomeric form of SWEET is functional; however, the effects of oligomerization on the transport activity remain elusive. Thus, future research should focus on understanding the effect of SWEET oligomerization and how it plays a role in sugar translocation.

METHODS AND MATERIALS

Simulation Details. The 3D coordinates of Oryza sativa OsSWEET2b (PDB ID: 5CTH) were downloaded from the Protein Data Bank (PDB).³² The membrane-protein molecular dynamics (MD) system was built using the Membrane Builder plugin in CHRMM-GUI. 33,34 The OsSWEET2b structure was aligned to the z-axis, inserted to a homogeneous phosphatidylcholine (POPC) lipid bilayer, and solvated using TIP3P35 water molecules. Although the plant membrane is heterogeneous, we preferred to use phosphatidylcholine (POPC) in our study, as the phospholipid composition of monocots shows a preference to PC as compared to other lipids in leaves, fruits, and grains. 36,37 We also noticed a similar pattern in dicots and in the model plant Arabidopsis thaliana. 38,39 Plant membranes have a wide array of sterols, but there is no known sterol binding site for SWEETs. It is well-documented that in the presence of sterols, the composition of lipids affects the protein dynamics by altering the membrane thickness. 40 Recent MD studies on bacterial SemiSWEETs were performed using membranes with homogeneous PC and mixed PE-PG lipids. We wanted to contrast the glucose transport mechanism of SWEETs and SemiSWEETs in this study, so we chose to maintain a similar lipid composition. Moreover, the studies on bacterial transporter, LacY, reveal that the substrate binding and transport rate do not vary significantly for different lipid environments. 41,42 Likewise, the computational study on another bacterial transporter, LeuT, in a different membrane environment shows that the average hydrophobic thickness does not vary significantly with lipid composition. 43,44 Therefore, we do not expect the nonspecific effects of membrane composition to significantly affect our results. The effect of different lipids on SWEETs and SemiSWEETs conformational dynamics is beyond the scope of the current study. However, it presents an interesting question about the role of plant lipids in altering membrane-protein function which could be addressed in a future work. The MD system was neutralized by adding a 150 mM NaCl salt concentration. The glucose molecule was added to a CHARMM-GUI built MD system using Packmol.⁴⁵ A 100 mM concentration of glucose (equivalent to 16 molecules) was randomly added to the MD system. Later, the MD system was saved as a pdb file format and used as an input in the Tleap module of AMBER 14⁴⁶ to convert from CHARMM to an amber force field file. The force field parameters for glucose were obtained from the GLYCAM database.⁴⁷ The amberff14SB force field was used for the MD simulation. 48 The MD system was subjected to conjugate gradient minimization for 20 000 cycles. Later, the system was slowly heated from 0 to 10 K in the NVT ensemble for 1 ns and from 10 to 300 K over a period of 2 ns in the NPT ensemble. The MD system was equilibrated for 50 ns at 300 K under the NPT condition. The temperature was maintained constant using the Berendsen thermostat, and pressure was maintained at 1 atm using a Berendsen barostat. 49 Hydrogen bonds were constrained using the SHAKE⁵⁰ algorithm, and long-range electrostatics were treated using the Particle Mesh Ewald method.⁵¹ The final production runs were conducted over a period of \sim 213 μ s.

We used an adaptive sampling approach for investigating the glucose transport process in OsSWEET2b. After each round of simulations, the simulation data were clustered on the basis of biologically relevant metrics, and the structures from the least populated clusters were chosen for the next round of simulation. This method increases the sampling efficiency by reducing the simulation time spent in the stable minima. 52 The trajectories were featurized on extracellular and intracellular gating residue distance and clustered using the minibatch Kmeans algorithm. 53 For the glucose bound simulation, we also included the z-position of glucose for clustering to improve the sampling of glucose bound states. The structures from the least populated clusters were chosen as starting structures to continue the next set of simulations, thereby improving the sampling of poorly sampled regions of configurational space. Adaptive sampling has been shown to efficiently sample the large conformational changes in various important targets. 54-60 The adaptive sampling approach introduces sampling bias in the simulation data set, and this bias is eliminated during construction of the Markov state model (MSM). The sampling bias is introduced as simulations are started from the least populated states after each round. Therefore, the population of the states based on the raw simulation data could be different form the real equilibrium population of the state. This issue is addressed by estimating the reversible transition probability matrix for transition between all of the conformational states. In the limit of large data, these errors are expected to be small.

Here, we show that there is not much difference between the population of states derived from raw data and the MSM derived equilibrium population. The list of the number of rounds of simulation for the glucose unbound and glucose bound simulation is given in Tables S1 and S2.

MSM Construction. The trajectory data were featurized on the basis of the 9 residue-residue contacts (Figure S1). The multidimensional data were transformed to the space of the 3 slowest time structure-based independent components (tICs) and clustered using the minibatch K-means algorithm.⁵³ The optimum cluster number was chosen using Osprey that generates the cross-validated generalized matrix Rayleigh quotient (GMRQ) score. 61 The highest scored cluster number, 900, was used for future analysis (Figures S2 and S3).62 MSMBuilder 3.6 was used to build MSM on trajectory data. 63 MSM was constructed using a lag time of 13 and 18 ns for glucose unbound and bound simulations. To check the quality of MSM, we estimated the error by a bootstrapping method that changes the underlying transition probability matrix, builds a new MSM, and estimates the free energy landscapes for the new MSM. We calculated the error for each bin of the 2D histogram to obtain the error bar on the conformational landscape plots. For both apo and holo MSM, the error bars lie in the range 0-0.5 kcal/mol. High values (0.5 kcal/mol) of error are only observed for low populated states at the edges of the landscapes. The average error in the free energy for all the bins is 0.2 kcal/mol (Figure S4). The equilibrium probability of all MSM states and raw count populations are shown in Table S3 and Figure S5. The conformational landscape for both apo and holo raw data with relative free energies is shown in Figure S6, and the plots are very similar to MSM weighted plots. The TPT module in MSMBuilder 3.6 was used to identify the conformational transition between the intermediate states. 19 The source (IF) and the sink (OF) states were chosen, and TPT identifies the top flux pathways through key intermediate states. Since it is hard to visualize and interpret 900 clusters to understand the conformational pathway, we lump MSM states into 6 macrostates. We analyzed macrostates and explained in detail how the crucial residues form key interactions to drive the structural transition from one state to the other. The kinetic plots are generated using Kinetic Monte Carlo. The Kinetic Monte Carlo synthetic trajectory shows state-to-state dynamics to characterize the glucose transition from the extracellular side to cytosol. Given a state i for a chosen lag time of 18 ns, the transition to state j was determined in MSM states. From each state the random snapshot was extracted, and a trajectory was obtained which is comparable to a single copy of the long simulation. We have chosen the glucose unbound OF state as a starting state and generated the 10 μ s trajectory to visualize the complete glucose

Trajectory Analysis. The CPPTRAJ module⁶⁴ in AMBER 14 and MDTRAJ⁶⁵ was used for postprocessing the MD trajectories. The 2D plots were generated using Matlab v2015 (MathWorks).⁶⁶ The MD snapshots were visualized and analyzed using VMD 1.9.2⁶⁷ and pymol v1.7.⁶⁸ To measure the pore radius of different states, we randomly extracted 300 frames from each state (OC and OF) from the simulation data, and the transport pore channel radius was calculated using the Hole program.²²

Yeast Complementation Growth Assay. SWEET1 mutants were made by overlapping PCR or synthesis. They were cloned into the yeast expression vector pDRf1-GW. Yeast

growth assays were carried out as described previously with minor changes. The hexose transporter deficient yeast strain EBY4000 [hxt1-17D::loxP gal2D::loxP stl1D::loxP agt1D::loxP ydl247wD::loxP yjr160cD::loxP] was used for transformation with vector (negative control), SWEET1 (positive control), and mutants, respectively. For spotting assays, cells were grown in liquid synthetic medium (0.17% YNB and 0.5% (NH₄)₂SO₄) with 2% maltose and then diluted to an OD600 of 0.1 in water. Three 10-fold serial dilutions were performed. The diluted yeasts were plated on synthetic medium containing either 2% maltose (as a control) or 2% glucose. Yeast growth was documented by Gel Doc (Biorad) after 3 days at 28 °C. No unexpected or unusually high safety hazards were encountered in this work.

ASSOCIATED CONTENT

S Supporting Information

The Supporting Information is available free of charge on the ACS Publications website at DOI: 10.1021/acscents-ci.9b00252.

Additional data and figures including structures, GMRQ scores, implied time scales plots, raw counts and MSM weighted data, conformation landscapes, transition path theory analysis, Kinetic Monte Carlo synthetic trajectory, and evolutionary sequence analysis (PDF)

AUTHOR INFORMATION

Corresponding Author

*E-mail: diwakar@illinois.edu.

ORCID 4

Ya-Chi Yu: 0000-0002-6937-0179 Diwakar Shukla: 0000-0003-4079-5381

Author Contributions

D.S. conceived and supervised the project. B.S. performed simulation. B.S. and D.S. analyzed the data. Y.-C.Y. and L.-Q.C. performed biochemical experiments. B.S. wrote the manuscript with input from D.S., Y.-C.Y., and L.-Q.C.

Notes

The authors declare no competing financial interest.

ACKNOWLEDGMENTS

Authors thank the Blue Waters sustained-petascale computing project, which is supported by the National Science Foundation (Awards OCI-0725070 and ACI-1238993) and the state of Illinois. D.S. acknowledges support from the New Innovator Award from the Foundation for Food and Agriculture Research and NSF Early Career Award (MCB 1845606). L.-Q.C. and Y.-C.Y. were supported by a startup fund from Department of Plant Biology, University of Illinois, Urbana—Champaign, IL. We thank Mathew Chan for making the cover art image for the article.

REFERENCES

(1) Lin, I. W.; Sosso, D.; Chen, L.-Q.; Gase, K.; Kim, S.-G.; Kessler, D.; Klinkenberg, P. M.; Gorder, M. K.; Hou, B.-H.; Qu, X.-Q.; Carter, C. J.; Baldwin, I. T.; Frommer, W. B. Nectar Secretion Requires Sucrose Phosphate Synthases and the Sugar Transporter SWEET9. *Nature* **2014**, *508*, 546–549.

(2) Sosso, D.; Luo, D.; Li, Q.-B.; Sasse, J.; Yang, J.; Gendrot, G.; Suzuki, M.; Koch, K. E.; McCarty, D. R.; Chourey, P. S.; Rogowsky, P. M.; Ross-Ibarra, J.; Yang, B.; Frommer, W. B. Seed Filling In

Domesticated Maize and Rice Depends on SWEET-Mediated Hexose Transport. *Nat. Genet.* **2015**, 47, 1489–1493.

- (3) Sun, M.-X.; Huang, X.-Y.; Yang, J.; Guan, Y.-F.; Yang, Z.-N. Arabidopsis RPG1 Is Important for Primexine Deposition and Functions Redundantly With RPG2 for Plant Fertility at the Late Reproductive Stage. *Plant Reprod.* **2013**, *26*, 83–91.
- (4) Chen, L.-Q.; et al. Sugar Transporters for Intercellular Exchange and Nutrition of Pathogens. *Nature* **2010**, *468*, 527–532.
- (5) Chen, L.-Q.; Qu, X.-Q.; Hou, B.-H.; Sosso, D.; Osorio, S.; Fernie, A. R.; Frommer, W. B. Sucrose Efflux Mediated by SWEET Proteins as a Key Step for Phloem Transport. *Science* **2012**, *335*, 207–211.
- (6) Chen, L.-Q. SWEET Sugar Transporters for Phloem Transport and Pathogen Nutrition. *New Phytol.* **2014**, 201, 1150–1155.
- (7) Wang, L.; Lu, Q.; Wen, X.; Lu, C. Enhanced Sucrose Loading Improves Rice Yield by Increasing Grain Sizee. *Plant Physiol.* **2015**, *169*, 15-01170.
- (8) Wang, J.; Yan, C.; Li, Y.; Hirata, K.; Yamamoto, M.; Yan, N.; Hu, Q. Crystal Structure of a Bacterial Homologue of SWEET Transporters. *Cell Res.* **2014**, 24, 1486–1489.
- (9) Xu, Y.; Tao, Y.; Cheung, L. S.; Fan, C.; Chen, L.-Q.; Xu, S.; Perry, K.; Frommer, W. B.; Feng, L. Structures of Bacterial Homologues of SWEET Transporters in Two Distinct Conformations. *Nature* **2014**, *515*, 448–452.
- (10) Lee, Y.; Nishizawa, T.; Yamashita, K.; Ishitani, R.; Nureki, O. Structural Basis for the Facilitative Diffusion Mechanism by SemiSWEET Transporter. *Nat. Commun.* **2015**, *6*, 6112.
- (11) Feng, L.; Frommer, W. B. Structure and Function of SemiSWEET and SWEET Sugar Transporters. *Trends Biochem. Sci.* **2015**, *40*, 480–486.
- (12) Pattison, R. J. Characterisation of the PQ-Loop Repeat Membrane Protein Family in Arabidopsis Thaliana. Ph.D. Thesis, University of Glasgow, 2008; pp 1–221.
- (13) Latorraca, N. R.; Fastman, N. M.; Venkatakrishnan, A.; Frommer, W. B.; Dror, R. O.; Feng, L. Mechanism of Substrate Translocation in an Alternating Access Transporter. *Cell* **2017**, *169*, 96–107.
- (14) Jardetzky, O. Simple Allosteric Model for Membrane Pumps. *Nature* **1966**, 211, 969–970.
- (15) Tao, Y.; Cheung, L. S.; Li, S.; Eom, J.-S.; Chen, L.-Q.; Xu, Y.; Perry, K.; Frommer, W. B.; Feng, L. Structure of a Eukaryotic SWEET Transporter in a Homotrimeric Complex. *Nature* **2015**, *527*, *259*–263
- (16) Han, L.; Zhu, Y.; Liu, M.; Zhou, Y.; Lu, G.; Lan, L.; Wang, X.; Zhao, Y.; Zhang, X. C. Molecular Mechanism of Substrate Recognition and Transport by the AtSWEET13 Sugar Transporter. *Proc. Natl. Acad. Sci. U. S. A.* **2017**, *114*, 10089–10094.
- (17) Berezhkovskii, A.; Hummer, G.; Szabo, A. Reactive Flux and Folding Pathways in Network Models of Coarse-Grained Protein Dynamics. *J. Chem. Phys.* **2009**, *130*, 205102.
- (18) E, W.; Vanden-Eijnden, E. Towards a Theory of Transition Paths. J. Stat. Phys. 2006, 123, 503-523.
- (19) Metzner, P.; Schutte, C.; Vanden-Eijnden, E. Transition Path Theory for Markov Jump Processes. *Multiscale Model. Simul.* **2009**, *7*, 1192–1219.
- (20) Machtens, J.-P.; Kortzak, D.; Lansche, C.; Leinenweber, A.; Kilian, P.; Begemann, B.; Zachariae, U.; Ewers, D.; de Groot, B. L.; Briones, R.; Fahlke, C. Mechanisms of Anion Conduction by Coupled Glutamate Transporters. *Cell* **2015**, *160*, 542–553.
- (21) Cao, Y.; et al. Crystal Structure of a Potassium Ion Transporter, TrkH. *Nature* **2011**, *471*, 336–340.
- (22) Smart, O.; Goodfellow, J.; Wallace, B. The Pore Dimensions of Gramicidin A. *Biophys. J.* **1993**, *65*, 2455–2460.
- (23) GetContacts. https://getcontacts.github.io/ (accessed Aug 31, 2018).
- (24) Xuan, Y. H.; Hu, Y. B.; Chen, L.-Q.; Sosso, D.; Ducat, D. C.; Hou, B.-H.; Frommer, W. B. Functional Role of Oligomerization for Bacterial and Plant SWEET Sugar Transporter Family. *Proc. Natl. Acad. Sci. U. S. A.* **2013**, *110*, E3685–E3694.

(25) Jia, B.; Zhu, X. F.; Pu, Z. J.; Duan, Y. X.; Hao, L. J.; Zhang, J.; Chen, L.-Q.; Jeon, C. O.; Xuan, Y. H. Integrative View of the Diversity and Evolution of SWEET and SemiSWEET Sugar Transporters. *Front. Plant Sci.* **2017**, *8*, 2178.

- (26) Celniker, G.; Nimrod, G.; Ashkenazy, H.; Glaser, F.; Martz, E.; Mayrose, I.; Pupko, T.; Ben-Tal, N. ConSurf: Using Evolutionary Data to Raise Testable Hypotheses about Protein Function. *Isr. J. Chem.* **2013**, *53*, 199–206.
- (27) Pietropaolo, A.; Pierri, C. L.; Palmieri, F.; Klingenberg, M. The switching mechanism of the mitochondrial ADP/ATP carrier explored by free-energy landscapes. *Biochim. Biophys. Acta, Bioenerg.* **2016**, *1857*, 772–781.
- (28) Gur, M.; Zomot, E.; Cheng, M. H.; Bahar, I. Energy landscape of LeuT from molecular simulations. *J. Chem. Phys.* **2015**, *143*, 243134.
- (29) Bera, I.; Klauda, J. B. Structural Events in a Bacterial Uniporter Leading to Translocation of Glucose to the Cytosol. *J. Mol. Biol.* **2018**, 430, 3337–3352.
- (30) Park, M.-S. Molecular Dynamics Simulations of the Human Glucose Transporter GLUT1. *PLoS One* **2015**, *10*, No. e0125361.
- (31) Fu, X.; Zhang, G.; Liu, R.; Wei, J.; Zhang-Negrerie, D.; Jian, X.; Gao, Q. Mechanistic Study of Human Glucose Transport Mediated by GLUT1. *J. Chem. Inf. Model.* **2016**, *56*, 517–526.
- (32) Berman, H. M.; et al. The Protein Data Bank. Acta Crystallogr., Sect. D: Biol. Crystallogr. 2002, 58, 899-907.
- (33) Jo, S.; Kim, T.; Iyer, V. G.; Im, W. CHARMM-GUI: A webbased graphical user interface for CHARMM. *J. Comput. Chem.* **2008**, 29, 1859–1865.
- (34) Lee, J.; et al. CHARMM-GUI Input Generator for NAMD, GROMACS, AMBER, OpenMM, and CHARMM/OpenMM Simulations Using the CHARMM36 Additive Force Field. *J. Chem. Theory Comput.* **2016**, *12*, 405–413.
- (35) Jorgensen, W. L.; Chandrasekhar, J.; Madura, J. D.; Impey, R. W.; Klein, M. L. Comparison of Simple Potential Functions for Simulating Liquid Water. *J. Chem. Phys.* **1983**, *79*, 926–935.
- (36) Zhang, C.; Hicks, G.; Raikhel, N. Molecular Composition of Plant Vacuoles: Important but Less Understood Regulations and Roles of Tonoplast Lipids. *Plants* **2015**, *4*, 320–333.
- (37) Yoshida, H.; Tanigawa, T.; Kuriyama, I.; Yoshida, N.; Tomiyama, Y.; Mizushina, Y. Variation in Fatty Acid Distribution of Different Acyl Lipids in Rice (Oryza sativa L.) Brans. *Nutrients* **2011**, 3, 505–514.
- (38) Yuan, M.; Wang, S. Rice MtN3/Saliva/SWEET Family Genes and Their Homologs in Cellular Organisms. *Mol. Plant* **2013**, *6*, 665–674.
- (39) Li, A.; Wang, D.; Yu, B.; Yu, X.; Li, W. Maintenance or Collapse: Responses of Extraplastidic Membrane Lipid Composition to Desiccation in the Resurrection Plant Paraisometrum mileense. *PLoS One* **2014**, *9*, No. e103430.
- (40) Jensen, M. Ø.; Mouritsen, O. G. Lipids do influence protein function—the hydrophobic matching hypothesis revisited. *Biochim. Biophys. Acta, Biomembr.* **2004**, *1666*, 205–226.
- (41) Seto-Young, D.; Chen, C.-C.; Wilson, T. H. Effect of different phospholipids on the reconstitution of two functions of the lactose carrier of Escherichia coli. *J. Membr. Biol.* **1985**, *84*, 259–267.
- (42) Vitrac, H.; Bogdanov, M.; Dowhan, W. Proper Fatty Acid Composition Rather than an Ionizable Lipid Amine Is Required for Full Transport Function of Lactose Permease from Escherichia coli. *J. Biol. Chem.* **2013**, 288, 5873–5885.
- (43) Mondal, S.; Khelashvili, G.; Shi, L.; Weinstein, H. The cost of living in the membrane: A case study of hydrophobic mismatch for the multi-segment protein LeuT. *Chem. Phys. Lipids* **2013**, *169*, 27–38
- (44) Pantano, D. A.; Klein, M. L. Characterization of Membrane-Protein Interactions for the Leucine Transporter fromAquifex aeolicusby Molecular Dynamics Calculations. *J. Phys. Chem. B* **2009**, 113, 13715–13722.
- (4S) Martínez, L.; Andrade, R.; Birgin, E. G.; Martínez, J. M. PACKMOL: A package for building initial configurations for

molecular dynamics simulations. J. Comput. Chem. 2009, 30, 2157–2164.

- (46) Case, D. A. et al. Amber 14; University of California: San Francisco, 2014.
- (47) Kirschner, K. N.; Yongye, A. B.; Tschampel, S. M.; González-Outeiriño, J.; Daniels, C. R.; Foley, B. L.; Woods, R. J. GLYCAM06: A Generalizable Biomolecular Force Field. Carbohydrates. *J. Comput. Chem.* **2008**, *29*, 622–655.
- (48) Maier, J. A.; Martinez, C.; Kasavajhala, K.; Wickstrom, L.; Hauser, K. E.; Simmerling, C. ff14SB: Improving the Accuracy of Protein Side Chain and Backbone Parameters From ff99SB. *J. Chem. Theory Comput.* **2015**, *11*, 3696–3713.
- (49) Berendsen, H. J. C.; Postma, J. P. M.; van Gunsteren, W. F.; DiNola, A.; Haak, J. R. Molecular Dynamics With Coupling to an External Bath. *J. Chem. Phys.* **1984**, *81*, 3684–3690.
- (50) Krautler, V.; van Gunsteren, W. F.; Hunenberger, P. H. A Fast SHAKE Algorithm to Solve Distance Constraint Equations for Small Molecules in Molecular Dynamics Simulations. *J. Comput. Chem.* **2001**, 22, 501–508.
- (51) Essmann, U.; Perera, L.; Berkowitz, M. L.; Darden, T.; Lee, H.; Pedersen, L. G. A Smooth Particle Mesh Ewald Method. *J. Chem. Phys.* **1995**, *103*, 8577–8593.
- (52) Bowman, G. R.; Ensign, D. L.; Pande, V. S. Enhanced Modeling via Network Theory: Adaptive Sampling of Markov State Models. *J. Chem. Theory Comput.* **2010**, *6*, 787–794.
- (53) Sculley, D. In *Web-scale k-means clustering*, Proceedings of the 19th International Conference on World Wide Web; 2010; pp 1177–1178
- (54) Selvam, B.; Mittal, S.; Shukla, D. Free Energy Landscape of the Complete Transport Cycle in a Key Bacterial Transporter. *ACS Cent. Sci.* **2018**, *4*, 1146–1154.
- (55) Shukla, D.; Meng, Y.; Roux, B.; Pande, V. S. Activation Pathway of Src Kinase Reveals Intermediate States As Targets for Drug Design. *Nat. Commun.* **2014**, *5*, 3397.
- (56) Kohlhoff, K. J.; Shukla, D.; Lawrenz, M.; Bowman, G. R.; Konerding, D. E.; Belov, D.; Altman, R. B.; Pande, V. S. Cloud-Based Simulations on Google Exacycle Reveal Ligand Modulation of GPCR Activation Pathways. *Nat. Chem.* **2014**, *6*, 15–21.
- (57) Selvam, B.; Shamsi, Z.; Shukla, D. Universality of the Sodium Ion Binding Mechanism in Class A G-Protein-Coupled Receptors. *Angew. Chem., Int. Ed.* **2018**, *57*, 3048–3053.
- (58) Moffett, A. S.; Bender, K. W.; Huber, S. C.; Shukla, D. Allosteric Control of a Plant Receptor Kinase through S-Glutathionylation. *Biophys. J.* **2017**, *113*, 2354–2363.
- (59) Moffett, A. S.; Bender, K. W.; Huber, S. C.; Shukla, D. Molecular dynamics simulations reveal the conformational dynamics of *Arabidopsis thaliana* BRI1 and BAK1 receptor-like kinases. *J. Biol. Chem.* **2017**, 292, 12643–12652.
- (60) Shukla, S.; Zhao, C.; Shukla, D. Dewetting Controls Plant Hormone Perception and Initiation of Drought Resistance Signaling. *Structure* **2019**, *27*, 692–702.
- (61) McGibbon, R. T.; Hernández, C. X.; Harrigan, M. P.; Kearnes, S.; Sultan, M. M.; Jastrzebski, S.; Husic, B. E.; Pande, V. S. Osprey: Hyperparameter Optimization for Machine Learning. *Journal of Open Source Software* **2016**, *1*, 34.
- (62) McGibbon, R. T.; Pande, V. S. Variational Cross-Validation of Slow Dynamical Modes in Molecular Kinetics. *J. Chem. Phys.* **2015**, 142, 124105.
- (63) Beauchamp, K. A.; Bowman, G. R.; Lane, T. J.; Maibaum, L.; Haque, I. S.; Pande, V. S. MSMBuilder2: Modeling Conformational Dynamics on the Picosecond to Millisecond Scale. *J. Chem. Theory Comput.* **2011**, *7*, 3412–3419.
- (64) Roe, D. R.; Cheatham, T. E. PTRAJ and CPPTRAJ: Software for Processing and Analysis of Molecular Dynamics Trajectory Data. *J. Chem. Theory Comput.* **2013**, *9*, 3084–3095.
- (65) McGibbon, R. T.; Beauchamp, K. A.; Harrigan, M. P.; Klein, C.; Swails, J. M.; Hernández, C. X.; Schwantes, C. R.; Wang, L.-P.; Lane, T. J.; Pande, V. S. MDTraj: A Modern Open Library for the

Analysis of Molecular Dynamics Trajectories. *Biophys. J.* **2015**, *109*, 1528–1532.

- (66) MATLAB, Version R2015b; MathWorks Inc.: Natick, MA, 2015.
- (67) Humphrey, W.; Dalke, A.; Schulten, K. VMD: Visual Molecular Dynamics. *J. Mol. Graphics* **1996**, *14*, 33–38.
- (68) PyMOL Molecular Graphics System, Version 1.7; Schrödinger, LLC., 2015.